

A computational model of *in vitro* angiogenesis based on extracellular matrix fibre orientation

Lowell T. Edgar^a, Scott C. Sibole^a, Clayton J. Underwood^a, James E. Guilkey^b and Jeffrey A. Weiss^{a*}

^aDepartment of Bioengineering & Scientific Computing and Imaging Institute, University of Utah, 72 South Central Campus Drive, Rm. 2646, Salt Lake City, UT 84112, USA; ^bDepartment of Mechanical Engineering & Scientific Computing and Imaging Institute, University of Utah, Salt Lake City, UT, USA

(Received 11 August 2011; final version received 29 January 2012)

Recent interest in the process of vascularisation within the biomedical community has motivated numerous new research efforts focusing on the process of angiogenesis. Although the role of chemical factors during angiogenesis has been well documented, the role of mechanical factors, such as the interaction between angiogenic vessels and the extracellular matrix, remains poorly understood. *In vitro* methods for studying angiogenesis exist; however, measurements available using such techniques often suffer from limited spatial and temporal resolutions. For this reason, computational models have been extensively employed to investigate various aspects of angiogenesis. This paper outlines the formulation and validation of a simple and robust computational model developed to accurately simulate angiogenesis based on length, branching and orientation morphometrics collected from vascularised tissue constructs. Microvessels were represented as a series of connected line segments. The morphology of the vessels was determined by a linear combination of the collagen fibre orientation, the vessel density gradient and a random walk component. Excellent agreement was observed between computational and experimental morphometric data over time. Computational predictions of microvessel orientation within an anisotropic matrix correlated well with experimental data. The accuracy of this modelling approach makes it a valuable platform for investigating the role of mechanical interactions during angiogenesis.

Keywords: angiogenesis; computational model; tissue engineering; extracellular matrix; fibre orientation; matrix anisotropy

1. Introduction

Angiogenesis, the process by which new blood vessels sprout off from existing vasculature, is highly sensitive to both the chemical and the mechanical microenvironment (Ingber 2002; Li et al. 2005; Shiu et al. 2005; Krishnan et al. 2008). During angiogenesis, endothelial cells within existing blood vessels detach from the basement membrane, migrate into the extracellular matrix (ECM) and form sprouts that elongate and eventually mature into new vasculature. Externally applied and cell-generated traction forces affect motility, metabolism, proliferation and differentiation of all anchorage-dependent cells, including endothelial cells and pericytes that participate in angiogenesis (Ives et al. 1986; Carosi et al. 1992; Patrick and McIntire 1995; Chien et al. 1998; Stamatias and McIntire 2001; McCormick et al. 2003; Joung et al. 2006). Mechanical stimuli received by cells via mechanotransduction depend on the structure and composition of the ECM (Vernon and Sage 1999; Deroanne et al. 2001), and on cell receptor structures bound to ECM components (Jalali et al. 2001).

The mechanism as to how mechanical forces, 3D boundary conditions and ECM structure/composition influence neovessel growth during angiogenesis is poorly

understood. Investigating this mechanism is difficult as the ECM is constantly remodelled and reorganised during angiogenesis through protease activity, formation of new cell–matrix adhesions and cellular force generation (Manoussaki et al. 1996; Krishnan et al. 2007). Overcoming these challenges and characterising the mechanical interactions between angiogenic microvessels and the ECM would not only provide new insight into the driving forces behind morphogenic processes, but also lead to new design considerations for engineering patterned microvasculature.

The role of mechanical factors during angiogenesis has been previously investigated *in vitro* using a novel 3D culture method (Krishnan et al. 2003, 2005, 2007, 2008, 2009). Using this method, sprouting occurs within microvessel fragments in a spontaneous and consistent manner. Sprouts elongate as patent tubes, branching and forming anastomoses with other vessels (Hoying et al. 1996; Shepherd et al. 2004). In free-floating constructs, microvascular networks were found to have no preferred orientation. When the vascularised constructs were subject to an applied strain or a boundary constraint, microvessels and collagen fibres were found aligned along the constrained axis (Krishnan et al. 2008). It is unclear if

*Corresponding author. Email: jeff.weiss@utah.edu

this alignment arises from microvessel growth being directed along aligned collagen fibres, from microvessels being reoriented due to contraction of the matrix and internal remodelling, or from some combination of both mechanisms.

Computational models can be utilised to supplement experimental efforts, often providing investigators with the ability to view systems at time points not sampled during the experiment or test hypotheses in ways not possible in the laboratory. Growth models have proven useful to investigators studying angiogenesis (Chaplain 2000; Mantzaris et al. 2004; Namy et al. 2004; Bauer 2007; Capasso et al. 2008; Qutub and Popel 2009). Computational frameworks can be categorised into different classes depending on how the system of interest is represented. Continuous models are typically governed by differential equations based on physical laws, whereas discrete models assemble a collection of discrete geometric units that behave according to a particular set of rules. Continuous–discrete models, or hybrid models, combine both approaches, often through determining the behaviour of discrete units by solving a problem governed by physical laws. A computational model capable of simulating the interaction between microvessels and the ECM during angiogenesis would be a valuable platform for studying the role of mechanical forces, matrix boundary conditions and ECM composition.

Vascular geometry can be captured in two ways: imaging data from vascularised constructs (specimen-specific data) and from computational predictions of microvessel growth. Since geometry obtained using the first method is constrained to the time point at which the culture was imaged, the second method was chosen as it provides a generalised description of microvascular geometry at any desired point in time. This paper proposes such a computational model of vessel growth designed to provide accurate, up-to-date microvascular geometry during *in vitro* angiogenesis. The model was designed using a continuous–discrete framework. This involves explicit representation of the microvessels as discrete structures with the ability to simulate elongation, branching and anastomosis over a regular computational grid. The continuous component of the model is in the differential equations used to govern field variables that influence neovessel growth. The growth model will also need to accurately predict the changes in microvessel growth resulting from ECM anisotropy and imposed boundary conditions as seen in the laboratory. The objectives of this study were to develop such a growth model and to demonstrate its ability to describe experimental data on microvessel length, branching and orientation obtained from vascularised constructs.

2. Methods

2.1 Cell culture experiments: *in vitro* model of angiogenesis

Morphometric data were collected from *in vitro* cultures of angiogenic microvessels in order to calibrate the computational growth model and to determine whether predictions from the simulation framework were valid. Based on previously described methods (Hoying et al. 1996), 38 microvessel cultures were prepared from five separate dissections. Microvessel fragments were isolated from epididymal fat pads harvested from retired breeder Sprague-Dawley rats while conforming to the Institutional Animal Care and Use Committee of the University of Utah. The fat pads were minced, digested with enzymes and subjected to sequential filtration. The filtration step allows the removal of large clumps of tissue as well as single cells from the suspension. The remaining filtrate was spun down in a centrifuge, and the resulting pellet consisted of microvessel fragments. Sterile rat tail type I collagen (BD Biosciences, Franklin Lakes, NJ, USA) was mixed with concentrated Dulbecco's modified Eagle medium (DMEM, GIBCO-Invitrogen, Carlsbad, CA, USA) to a density of 3.0 mg/ml collagen in $1 \times$ DMEM. The pellet of microvessel fragments was resuspended in the collagen/DMEM solution at a density of 15,000 fragments/ml, and the solution was transferred to circular culture wells (diameter ~ 15 mm). The collagen was allowed to polymerise at 37°C and 95% humidity for 30 min. Constructs were incubated in serum-free media (Bottenstein and Sato 1979) supplemented with rhVEGF (10 ng/ml, VEGF 165, PeproTech, Rocky Hill, NJ, USA). The constructs cast within the circular culture wells were free floating with no applied stretch or imposed boundary conditions, which created collagen fibres with no preferred orientation (random) [Figure 1(A),(B)]. Constructs were incubated at 37°C and 95% humidity for 7 days, after which the microvascular network within each construct was imaged using confocal microscopy.

To create the anisotropic ECM condition, five rectangular vascularised constructs were also prepared. These constructs were subjected to fixed-edge boundary conditions by allowing the collagen to polymerise within a stainless steel mesh, preventing contraction of the collagen gel along the long axis but leaving the rest of the gel free to contract [Figure 1(C),(D)]. This boundary condition produces microvessel and collagen fibril alignment along the long axis of the constructs (Krishnan et al. 2008). Microvessel orientation data were collected after 6 days of growth to compare with the simulation results. Collagen fibre orientation data were also collected to provide the fibre orientation information for the model when simulating the anisotropic matrix condition.

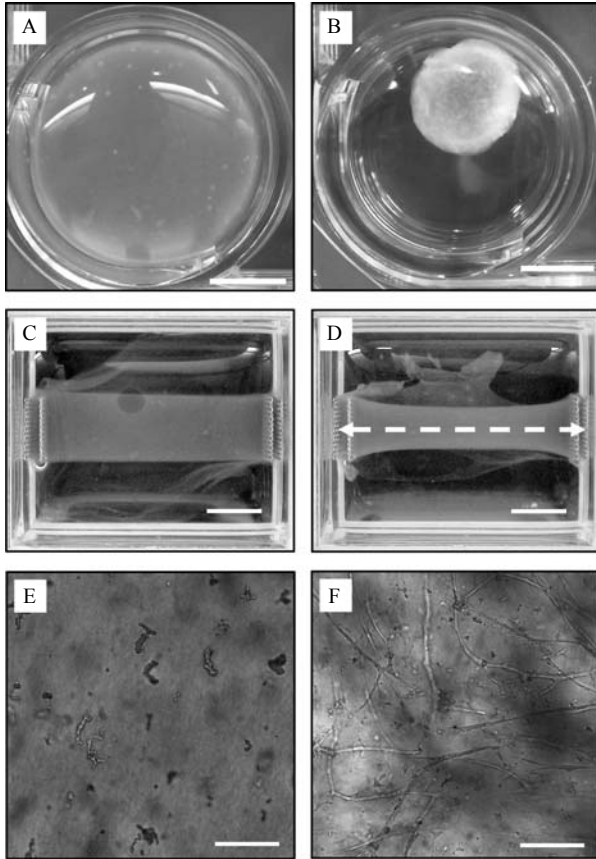


Figure 1. Microvessel cultures provided an *in vitro* model of angiogenesis used for validating the computational model. Collagen gels serving as the ECM were subjected to two different boundary conditions. (A) Round, free-floating culture at day 0. (B) After 6 days, free-floating gels were uniformly contracted by cellular traction forces. Scale bar = 5 mm. (C) Rectangular collagen gel with the long axis constrained at day 0. (D) After 6 days, the fixed-edge constructs contracted along the short axis, with the most contraction found at the centre of the gel (furthest point away from the boundary conditions). Microvessels and collagen fibres within these constructs were found predominately orientated along the constrained axis, shown as a white dashed line. Scale bar = 5 mm. (E) A $10\times$ light micrograph displaying initial microvessel fragments within a free-floating collagen gel at day 0. (F) Representative growth profile seen within a free-floating vascularised construct after 6 days of culture. Scale bar = $200\ \mu\text{m}$.

2.2 Image acquisition and processing

At the end of each culture period, the vascularised constructs were fixed with 4% formaldehyde overnight and then washed with phosphate-buffered saline containing 0.1% Triton X-100. Endothelial cells were stained with a $2\ \mu\text{g}/\text{ml}$ solution of isolectin IB₄-Alexa 488 conjugate (Invitrogen). Three-dimensional image data-sets of the stained microvessels were obtained using laser scanning confocal microscopy (Olympus FV1000 CLSM) utilising a 488 nm excitation laser and a $10\times$ objective. Six adjacent fields ($1.27\times 1.27\ \text{mm}$) were acquired about the

construct centre through a depth of $300\ \mu\text{m}$ from the bottom surface of the gel with a $2.5\ \mu\text{m}$ z -step interval. Individual image stacks were acquired at a resolution of $512\times 512\times 300$ voxels.

The image stacks for the six adjacent fields were stitched together using custom software. Unless specified, all other image processing was performed through Amira™ (Mercury Computer Systems, Carlsbad, CA, USA). A blind deconvolution (10 iterations) was performed on image stacks using a point spread function based on the numerical aperture ($\text{NA} = 0.4$, $10\times$, air), wavelength of light ($\lambda = 520\ \text{nm}$) and an estimate of the refractive index of the collagen gel ($n = 1.35$, Liu et al. 2006) to eliminate out-of-plane blur. Volume data were filtered to remove fragments smaller than $600\ \mu\text{m}^3$, as it was observed that objects below this size range were usually due to single cells, debris or noise and did not represent microvessels. Microvessel volumes were then reduced to line segments by a skeletonisation algorithm as previously described (Krishnan et al. 2007, 2008). A custom application was used to analyse the skeletonised data, and collect the total vessel length and number of branches in each culture (WinFiber3D). Although it is possible that some branch points may represent anastomoses, it was assumed that all branch points represent new branching of sprouts from the existing vessels. This is a reasonable assumption because anastomosis requires microvessels to be within close proximity of each other, and the topology of the microvascular network in this culture model primarily results from divergent growth (Krishnan et al. 2003, 2005, 2007, 2008, 2009).

2.3 Morphometric data: vascular length

A function describing microvessel growth over time was created from experimental data to define growth within the computational model. For each time point sampled, the length of all microvessels within the field was normalised by the initial number of microvessel fragments. The number of initial fragments was calculated from the seeding density used when preparing the cultures ($15,000\ \text{fragments}/\text{ml}$). This normalisation ensures that the growth mechanisms within the model are independent of the initial microvessel seeding density. Length metric data from each experiment were averaged across each of the free-floating cultures, and these data were fit with a four-parameter sigmoid curve:

$$g(t) = g_0 + \frac{a_1}{1 + e^{-[(t-t_{1/2})/b_1]}}. \quad (1)$$

This function describes the total vascular length within the domain at any point in time. A sigmoid curve was chosen to describe microvessel growth, as such a curve is often used to describe population growth restricted by

limited resources (carrying capacity). In Equation (1), g_0 is the initial microvessel length (bottom of the sigmoid curve), a_1 is the range of the function (top minus bottom), $t_{1/2}$ is the time at which $g(t)$ is halfway in between the top and bottom of the sigmoid curve and b_1 describes the steepness of the curve. The carrying capacity of the system can be described as $g_0 + a_1$.

2.4 Morphometric data: vascular branching

The computational model also required a function describing microvessel branching over time. For each time point, the number of branch points within the field was averaged together and normalised by the initial number of microvessel fragments. The branching $b(t)$ was calculated by fitting the average branching data with a three-parameter exponential curve:

$$b(t) = b_0 + a_2 e^{b_2 t}. \quad (2)$$

In this equation, b_0 describes the initial number of branches, a_2 scales the exponential term and b_2 describes the rate of branch formation. An exponential function was used to describe branch formation as branching metric data taken from experimental cultures does not appear to approach any limit during the 7-day culture period.

2.5 Collagen fibre orientation

The culture and imaging procedure described above were repeated for the five fixed-edge constructs at day 6 of culture. Measurements from these constructs included the angles for all microvessel segments relative to the constrained axis (long axis). The structural organisation of the underlying collagen matrix within the fixed-edge constructs was quantified by imaging collagen fibrils using confocal reflectance microscopy with a 60X water objective and a 633 nm laser. For each construct, two stacks were acquired through a depth of 120 μm with a 1- μm z -step interval. An orientation of collagen fibres was determined from the images by employing a 2D Fourier transform technique on each image (Pourdeyhimi et al. 1997; Sander and Barocas 2009). The angle distributions from the five cultures were averaged together and fit with a Gaussian distribution. This distribution was used to seed a vector field that represents an anisotropic matrix for the computational growth model.

2.6 Computational model: overview

The computational model of vessel growth during *in vitro* angiogenesis was calibrated and validated with data obtained using the methods described above. The formulation and implementation was 3D, although for

simplicity the simulations presented in this paper were only performed in two dimensions. The simulation domain, or virtual ECM, was discretised with a regular quadrilateral mesh with an element spacing of 31.75 μm in each direction. Local field information such as ECM collagen fibril orientation and microvessel density was specified at each of the grid nodes. At any position (x, y) , the field described at the nodes could be mapped to that point via bilinear shape functions:

$$\varphi(x, y) = \sum_{i=1}^4 S_i(x, y) \varphi_i, \quad (3)$$

where φ was a field variable and $S_i(x, y)$ were the values of the shape functions for each of the four nodes of the cell, evaluated at the point (x, y) ; Figure 2). This approach can be applied to include any field information deemed pertinent by the user. The dimensions of the domain were 1.27 \times 1.27 mm for all simulations, corresponding to the 10X field of view on the confocal microscope. Periodic boundary conditions were imposed on all edges of the simulation domain.

2.7 Computational model: vessel elongation

Initial microvessel fragments were represented as discrete independent line segments, with lengths corresponding to the value of the sigmoid growth curve $g(t)$ at time $t = 0$ (Equation (1)). Twenty-five fragments (average number in

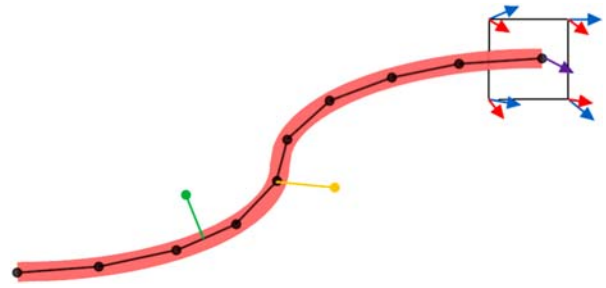


Figure 2. Microvessels were represented as a series of line segments. At each time step, neovessel growth occurred through the addition of a new line segment at the active tips of existing segments. The orientation of new segments was determined from information stored at the nodes of the grid cell. In this figure, the red and blue arrows represent directional cues determined by field information stored at the nodes. The red arrows are longer than the blue to represent the uneven weighting of various factors, i.e. collagen fibril direction was more influential than vessel density gradient. The direction of the new segment (purple arrow) was determined by interpolation of red and blue field variables via bilinear shape functions (Equation (3)). At each time step, a segment formed a branch if a random number was below a branching probability parameter. The yellow segment demonstrates a branch formation. Anastomoses can form anywhere along a microvessel where an intersection occurs, as shown by the green line segment.

the field of view of a confocal image) were seeded throughout the domain, each at a random position and with a random orientation.

At each time step, microvessel growth was represented by the addition of new segments to the free ends of existing segments. A variable time step was implemented to limit the growth of any vessel segment to half a grid cell. The length of each new segment was calculated by referencing the growth curve $g(t)$ and determining the change in length over the time step size (Equation (1)). With this method of vessel elongation, all vessels within the domain grow by the same amount at each time step. While this method may not accurately describe real growth of an individual neovessel, this method does provide valid predictions of microvascular topology in an averaged sense. The direction of new segments was determined by a linear combination of several directional cues. The orientation vector \mathbf{v} for a newly created segment was found using the following expression:

$$\mathbf{v} = w_1 \boldsymbol{\theta}_{\text{coll}} + w_2 \boldsymbol{\theta}_{\text{vdens}} + w_3 \boldsymbol{\theta}_{\text{rand}}. \quad (4)$$

In Equation (4), the vector $\boldsymbol{\theta}_{\text{coll}}$ was along the direction of local collagen fibres, the vector $\boldsymbol{\theta}_{\text{vdens}}$ was calculated from the vessel density gradient to cause microvessels to grow away from regions of high microvessel density, and the vector $\boldsymbol{\theta}_{\text{rand}}$ was a random walk component. The scalars w_1 , w_2 and w_3 were the weights for each of these components. Each of the directional components was determined by mapping field information stored at the nodes of the grid to the position of the new segment (Equation (3)).

2.8 Computational model: branching

Microvessel branching was modelled as a stochastic process. During each time step, each segment was assigned a random number between 0 and 1. Branching occurred when a segment's random number was less than a branching probability value:

$$B_t = \frac{B_0}{t} \Delta t \quad \text{if } \text{rand}[0, 1] \leq B_t, \text{ form a new branch} \quad (5)$$

else do not branch.

The initial branching probability, B_0 , value was determined using a golden section, single variable, bounded optimisation algorithm to minimise the root mean square (RMS) error between simulated and experimental length and branch metrics. This probability value was assigned to all initial fragments at $t = 0$ where Equation (5) is undefined. Multiplying by the time step Δt eliminated dependence of branching behaviour on time step size. Based on Equation (5), the branching probability for an individual line segment decreases as time increases.

This particular behaviour was chosen because the rate at which new segments formed in the model would otherwise far outpace the rate at which new branches were observed to form in the experimental cultures.

2.9 Computational model: anastomosis

Growth tips within close proximity to other microvessels were capable of forming anastomoses. At the end of each time step, a search for intersections between all active vessel tips and existing segments was conducted. If the intersection found was in between two segments within the same vessel, the intersection was ignored to avoid the formation of a terminal loop. If the intersecting segments were not from the same microvessel, a procedure was used to determine if they would intersect in three dimensions. This process is necessary because the model represented a 2D projection of vessels in 3D. In 3D, a microvessel could be positioned at any point throughout the culture thickness of 300 μm . To account for the 3D geometry, a test was performed based on the probability of the two microvessels being offset by less than 1 microvessel diameter in the third spatial dimension. This involved taking the ratio between the microvessel diameter and the culture thickness. If the random number was less than this ratio, the microvessels formed an anastomosis and ceased growth; otherwise, the intersection was ignored.

2.10 Computational model: optimisation of branching

A golden-section line search was used to determine the optimal value of B_0 within the branching mechanism (Equation (5)) by minimising the RMS error between simulated and experimental branching data:

$$\min \sum_{i=1}^n \sqrt{\frac{(\psi_e(t_i) - \psi_m(t_i))^2}{n}}. \quad (6)$$

Here, $\psi_e(t_i)$ was branching metric value from experimental data at a given time point t_i , $\psi_m(t_i)$ was the branching metric value from the computational simulations and n was the number of time steps taken.

2.11 Computational model: ECM anisotropy

The computational model was designed with the ability to simulate microvessel growth under various matrix boundary conditions. Different boundary conditions were modelled by changing the orientation of collagen fibrils within the matrix. For simulations involving a free-floating collagen gel, a random collagen fibre orientation angle between -90° and 90° was generated at each node of the grid. When simulating angiogenesis within the anisotropic

matrix condition, nodal collagen fibre orientation values were seeded using angle distributions collected from the fixed-edge constructs. The orientation of microvessels from these simulations was compared to orientation data from the fixed-edge constructs to verify the model's ability to predict angiogenesis within an anisotropic matrix.

2.12 Computational model: optimisation of vessel orientation

Microvessel orientation within the model was optimised to match experimental data. A routine similar to Equation (6) was used to determine the optimal values of the weights describing the strength of directional cues when determining the orientation of new microvessel segments (w_1, w_2, w_3) (Equation (4)). These weights were adjusted to minimise the RMS error between microvessel orientation in the fixed-edge constructs on day 6 and microvessel orientation from the anisotropic ECM simulations:

$$\min \sum_{i=1}^n \sqrt{\frac{(\phi_e(i) - \phi_m(i))^2}{n}}, \quad (7)$$

where $\phi_e(i)$ was the percentage of microvessels whose orientation angle fell into discrete angle bin i ($0^\circ-10^\circ, 10^\circ-20^\circ, \dots, 80^\circ-90^\circ$) measured off the constrained axis. $\phi_m(i)$ was the percentage of microvessels found in bin i from the simulations, and n was the number of discrete angle bins.

2.13 Computational model: variation due to stochastic processes

While microvessel elongation within the model was a deterministically governed process, the mechanisms for branching and anastomosis were stochastically based. Since branch formation and anastomosis directly affect the number of active growth tips, stochastic variations between different simulations can be passed from these random mechanisms to length metric data. To eliminate stochastic variations, growth rate was normalised by the number of active growth tips currently in the model. This adjustment ensures that the total length in each simulation will not vary too far away from the value prescribed by $g(t)$, reducing significant variation in length metric data over multiple simulations.

The seed used to initialise the random number generator algorithm prior to each simulation was varied based on the system clock. In order to assess the degree of variance across simulations caused by the stochastic processes, 50 simulations of microvessels growing within a randomly orientated ECM were conducted, each using a unique seed. The variance in the length and branch metrics

between these trials was then evaluated using a one-way ANOVA.

Variations in the simulation results due to the stochastic components of the model prevented convergence to strict tolerances ($\epsilon = 1e-7$) during the optimisation routines. Therefore, a constant seed was used while optimising individual parameters to facilitate convergence.

3. Results

Microvessel growth profiles were consistent across all *in vitro* experiments. Very little growth occurred before the 3–4 days mark, at which point sprouting was observed. Microvessels grew with a high rate until days 6–7, after which growth rate began to slow as the system neared its carrying capacity (Figure 3, top). The sigmoid curve fit to the averaged length metric data ($g(t)$, Equation (1)) resulted in an R^2 value of 0.998.

The number of branch points measured in the vascularised constructs increased exponentially throughout time with no observable limit during the 7-day culture period (Figure 3, bottom). The exponential curve fit to the averaged branch metric data ($b(t)$, Equation (2)) achieved an R^2 value of 0.968. The parameters determined from the curve fits can be found compiled in Table 1. Variance in length and branch metric data across *in vitro* cultures was high, with maximum standard deviations of 179.7 and 1.74, respectively.

Microvessel growth resulting from computational simulations resembled growth profiles seen *in vitro* (Figure 4). The length of microvascular networks from the computational simulations correlated well with experimental data, with approximately 1% normalised RMS error between computational and experimental length metric data (Figure 5, top). The optimisation routine used to determine the branching chance parameter returned a value of $B_0 = 0.038$ (Equation (5)). This branching parameter minimised the normalised RMS error between computational and experimental branching metric data to roughly 6% (Figure 5, bottom).

Microvessels within the fixed-edge constructs were found preferentially aligned along the constrained axis, consistent with what has been seen in past experiments (Krishnan et al. 2008). The majority of fibres in the fixed-edge constructs were found aligned along the constrained axis. The distributions of fibre angles for all five of the fixed-edge constructs were averaged together and fit to a Gaussian distribution which was used to generate a collagen fibre orientation at each node of the grid node (Figure 6).

Simulations of angiogenesis within a randomly orientated ECM produced microvessels with no preferential alignment, similar to what has been seen in free-floating

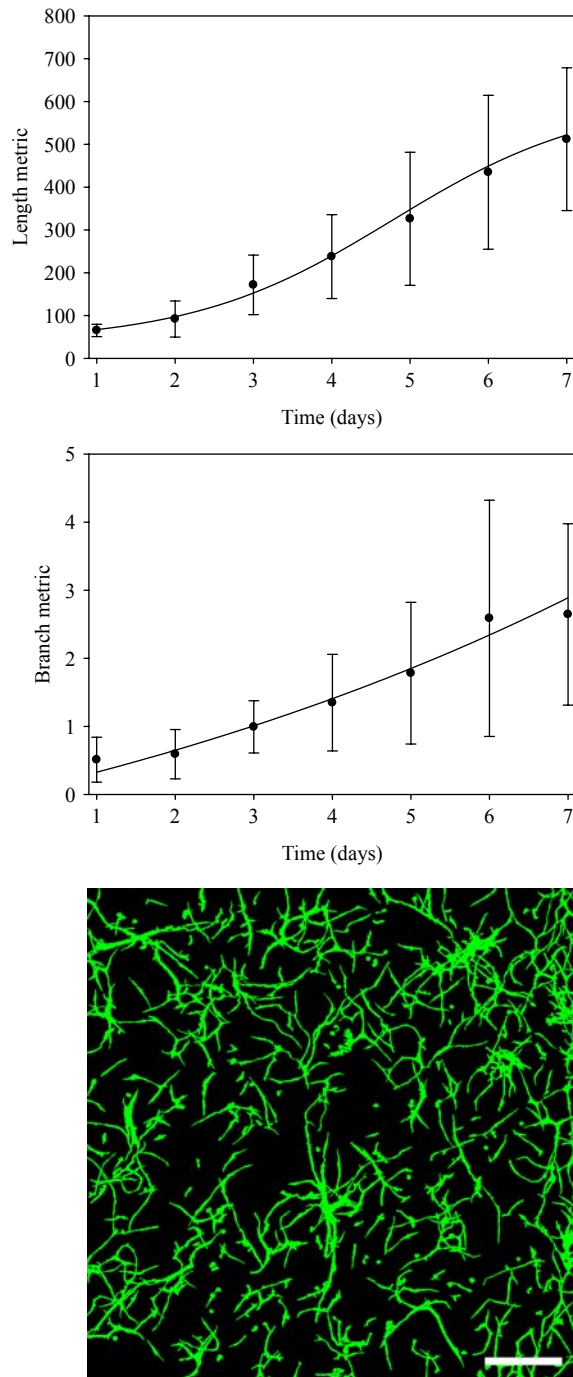


Figure 3. Morphometric data describe microvessel growth and branching during angiogenesis. (Top) Length metric data (current vessel length/number of vessels at day 1) versus time. The function $g(t)$ was fit to this data (Equation (1)). (Middle) Microvessel branch metric data (current number of branches/number of vessels at day 1) versus time. The function $b(t)$ was fit to this data (Equation (2)). In both the top and middle figures, points represent experimental data (mean \pm standard deviation) while solid curves represent regression fits. (Bottom) Z-projection of a representative microvessel culture. Image data were collected by imaging vascularised constructs at day 6 using a confocal microscope. Scale bar = 400 μm .

Table 1. Values of the parameters used for the growth function, branching function, branching probability and strength of directional queues.

Growth function $g(t)$	
a_1	568.6
g_0	38.8
b_1	1.3
$t_{1/2}$	4.8
Branching function $b(t)$	
y_0	-2.50
a_2	2.62
b_2	0.105
Branching probability	
B_0	0.038
Strength of directional cues	
w_1 fibre orientation	0.508
w_2 vessel density	0.238
w_3 random walk	0.254

Please see the text for the equations that define these functions and parameters.

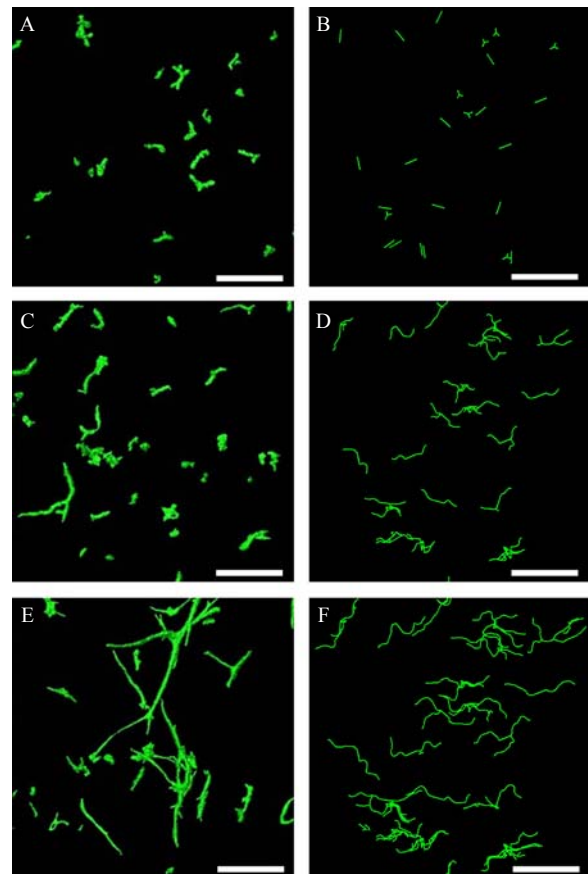


Figure 4. Images from computational simulations presented for comparison with experimental data. Confocal images from vascularised constructs are on the left, while data from simulations of microvessel growth can be found on the right. The time points at which these images were obtained are as follows: day 1 (A,B), day 4 (C,D) and day 7 (E,F). Scale bar = 300 μm . Predictions of microvasculature from the computational model were similar to images taken from vascularised constructs. Notice that growth predicted in the simulations followed a more tortuous path compared to microvessels *in vitro*.

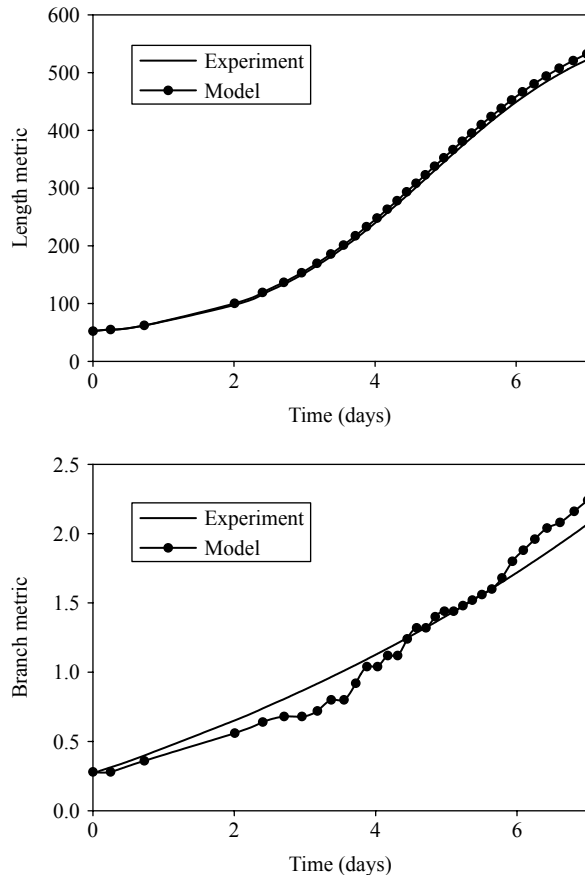


Figure 5. Computational simulations accurately predict experimental length and branching metric data taken from experimental cultures. (Top) Comparison of computational and experimental length metric data versus time. There was a normalised RMS error of approximately 1% between the two data-sets. (Bottom) Comparison of simulated and experimental branch metric data (number of current branches divided by initial number of microvessels in culture) versus time. There was a normalised RMS error of approximately 6% between the two data-sets.

vascularised constructs (Krishnan et al. 2008) (data not shown). The computational model was also successful at predicting angiogenesis within an anisotropic ECM. The angle between each microvessel and the long axis of the vascularised construct was measured from the simulations and constrained gel experiments. In both simulations and experiments, the majority of microvessels were found aligned within 20° of the constrained axis (Figure 7). Although significant differences exist between computational and experimental data for some of the angle bins, the correlation coefficient between the two data-sets was calculated to be $R^2 = 0.98$. The weights w_1 , w_2 and w_3 of the three-directional components described in Equation (4) were determined by optimising the orientation of microvessel segments within the computational model (Table 1).

To render length data from the simulations immune to these stochastic variations, the growth function $g(t)$ was normalised by the number of active growth tips within the simulation. This method was tested by observing the final length metric value over 50 simulations. For each of the 50 simulations, the final length metric value did not significantly vary from the value prescribed by $g(t)$ (Figure 8, top). In contrast, when the same test is performed for branch metric data, the number of branching points within the simulation varied significantly across 50 simulations (Figure 8, bottom).

4. Discussion

The continuous–discrete framework outlined in this paper was successful at predicting length and branching behaviour exhibited by angiogenic microvessels *in vitro*. Measurements of growth, branching and alignment metrics provided by simulations had excellent statistical agreement with experimental data. This accuracy was obtained through optimisation of only four parameters: the branching probability constant and the three weights influencing growth direction. Introducing additional parameters into the optimisation routine would lead to even greater predictive performance from the model, but the simple approach employed in this work satisfied the objectives of this study.

Orientation data from simulations of the anisotropic ECM condition correlated well with microvessel orientation observed in the fixed-edge vascularised constructs. However, angle data from the simulations tended to favour the acute angle bins more than the corresponding experimental data. Approximately 90% of microvessels from the simulations were found orientated between 0° and 45° off of the constrained axis. Only 80% of microvessels within the fixed-edge constructs fell within this same range. Although this difference is seemingly trivial, it is important to account for all inconsistencies between the model and *in vitro* findings. This particular inconsistency is important since the cornerstone assumption for this simulation framework is that microvessel growth follows collagen fibre orientation.

The inconsistency in microvessel orientation during simulations of the anisotropic ECM condition may be due to the assignment of an aligned ECM on day 0 of each simulation. Within the fixed-edge constructs, angiogenesis begins in a random ECM that is remodelled during vessel growth, resulting in an aligned matrix. In future simulations, supplying a fibril orientation field that can vary over time will allow the model to capture the transition to anisotropy that results from matrix remodelling. While the growth of angiogenic microvessels may follow matrix fibre growth orientation through contact guidance (Shiu et al. 2005; Krishnan et al. 2007, 2008), neovessels

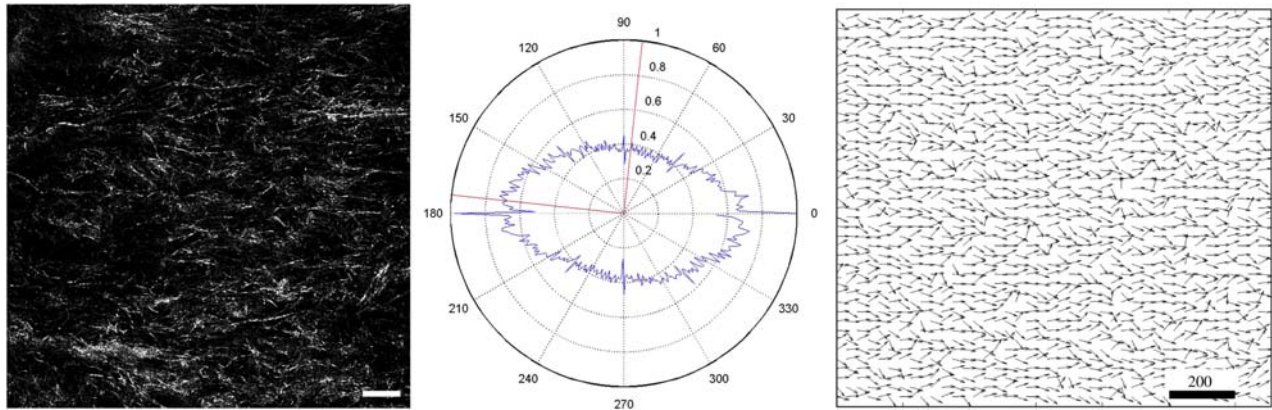


Figure 6. Anisotropic collagen fibril orientation was observed within the fixed-edge constructs. (Left) Confocal reflection microscopy image of collagen fibrils within a representative fixed-edge construct at day 6 *in vitro*. (Middle) Fast Fourier transform (FFT) analysis of collagen fibril data from constrained gels. Collagen fibrils were found to be predominately aligned along the constrained axis (0° – 180°). (Right) A field of collagen fibril angles based on angle distribution extracted from confocal reflectance microscopy images. This vector field was stored at the nodes of the grid in simulations of angiogenesis subjected to the anisotropic ECM condition. Scale bar = 200 μm .

may also alter local fibre orientation by applying traction forces to the ECM during growth. This leads to a coupling between angiogenic growth and matrix deformation, and it is difficult to separate these effects. In order to investigate this phenomenon, the authors plan to couple the computational model of vessel growth to a framework in solid mechanics that can predict deformation of the ECM during angiogenesis. However, the intricate nature of neovessel morphology makes it difficult to represent their geometry using traditional discretisation schemes in computational solid mechanics such as the finite element method. One possible approach to deal with representing the microvessel morphology was described in a recent study, using a particle-based method known as the material point method (MPM) (Sulsky et al. 1994, 1995). With this method, particle distributions can be generated from confocal microscopy image data-sets on a specimen-specific basis (Guilkey et al. 2005, 2006). The coupling of the growth model with simulations of solid mechanics will create a more realistic simulation of *in vitro* angiogenesis.

Although the simulations and experiments agreed statistically, there were qualitative discrepancies in the computational predictions of microvessel morphology. Simulated microvessel growth followed a more tortuous path compared to microvessels cultured in the laboratory. This discrepancy resulted from the mechanism used to determine the orientation of new segments within the computational model. New segments are allowed to form any angle with the parent vessel segment, leading to kinked microvessel morphology during elongation. Implementation of a persistence component into the vessel growth mechanism will make the microvessels resistant to changes in direction, ideally eliminating this morphological discrepancy.

The stochastic processes within the model led to minimal variation between simulations. Microvessel length was unaffected by the random numbers generated during the simulations. This independence from the random processes was expected as microvessel growth rate was normalised to account for the random formation of branches and anastomoses. However, some aspects of microvascular topology were sensitive to variations in the random number generator seed. Branching was governed by a stochastic process, and branches would form at different times and in different locations after re-seeding the random number generator. Likewise, the position and orientation of initial microvessel fragments would vary between random number generations as well. The conclusion is that these stochastic variations are small enough to not cause instabilities, yet pronounced enough to ensure that each simulation returns a unique microvascular network.

Future development of the computational framework will involve the replacement of stochastic components with deterministic mechanisms. For example, past mathematical models have suggested that steep gradients in collagen density local to a tip cell can induce the formation of a branch (Bauer 2007). Likewise, with further analysis of confocal image data, it may be possible to determine the degree of persistence involved during microvessel elongation. During the simulation, ECM collagen fibril orientation was supplied as an input parameter. Therefore, future simulations could easily predict *in vitro* angiogenesis for a given matrix orientation by simply mapping the desired fibril orientation field to the grid.

Chemical factors such as VEGF, TGF- β and PDGF play a vital role during angiogenesis (Shiu et al. 2005). In order to isolate and study the impact of

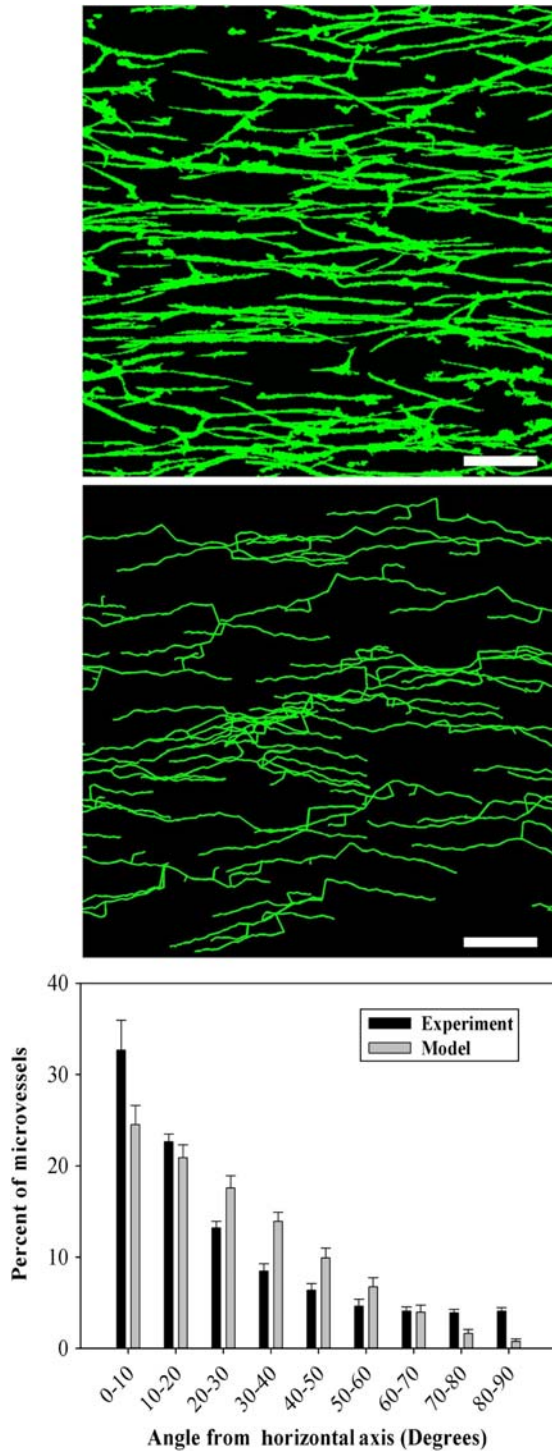


Figure 7. Computational simulations successfully predicted microvessel orientation within an anisotropic ECM. (Top) Microvessels cultured within the fixed-edge constructs were found predominately aligned along the constrained axis. (Middle) Computational simulations of angiogenesis occurring within an anisotropic ECM accurately predicted experimental findings. (Bottom) The angle between each microvessel segment and the horizontal axis was collected and sorted into discrete bins. Orientation data from the computational model correlated well with data from the fixed-edge vascularised constructs. Scale bar = 400 μm .

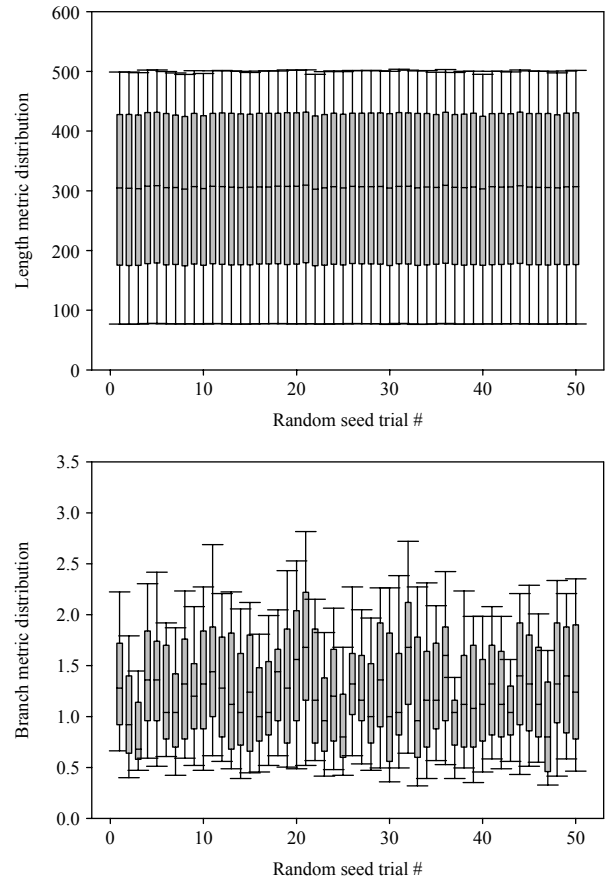


Figure 8. Stochastic variation within the computational simulations. Box-whisker plots of length (top) and branch (bottom) metric collected over 50 simulations, each with a unique P-RNG seeds. A one-way ANOVA was performed to check for significant variance between trials. No significant variation in the length metric was seen while varying the P-RNG seed ($p = 1.0$). Branching was modelled as a stochastic process, and therefore the branch metric significantly varied between trials ($p < 0.001$).

mechanical/structural stimuli during angiogenesis, the current model implementation does not include any chemotactic guidance during neovessel outgrowth. The *in vitro* system being modelled was uniformly immersed in VEGF, leaving only local synthesis of chemical factors as a possible source of chemical inhomogeneity. Rat tail type I collagen used for the experimental model does not contain trapped cytokines which can be released upon digestion (Assoian et al. 1983; Roberts et al. 1986). Therefore, it was possible to simulate *in vitro* angiogenesis accurately without including chemotaxis since significant chemotactic gradients do not develop within the vascularised constructs.

The algorithms described in this study were highly robust and efficient, with simulations completing within seconds. The model demonstrates forward compatibility through the ability to simulate different matrix boundary conditions and simple coupling to optimisation algorithms.

The growth model will provide the MPM algorithm with an accurate and current microvessel geometry that can be used to determine the state of stress/strain within microvessels and the surrounding matrix for any given point in time (Guilkey et al. 2006). Information about the deformation from the MPM simulations can then be used to update important information such as matrix fibre orientation, matrix density and vessel stretch. This information can be used to direct vessel growth in the next time step, and this process will repeat as both models step throughout time.

In summary, the simulation framework outlined in this work was capable of producing an accurate description of microvascular length, branching and orientation metrics over time for both an isotropic and anisotropic ECM fibril orientation field. The extent of angiogenesis can be tightly controlled by adjusting the input parameters, giving the model the ability to simulate a wide range of problems. Finally, the shape functions within the grid provide a basis for expanding the model to include additional field variables that influence neovessel growth and orientation. For example, stress/strain fields could be mapped to the nodes of the grid within the vessel growth model, effectively coupling stress and strain fields within the matrix to angiogenesis. These features allow this framework to serve as an effective platform for exploring how mechanical interactions between neovessels and the ECM regulate angiogenesis.

Acknowledgements

Financial support from NIH grants R01HL077683 and R01EB007556 is gratefully acknowledged.

References

- Assoian RK, Komoriya A, Meyers CA, Miller DM, Sporn MB. 1983. Transforming growth factor-beta in human platelets. Identification of a major storage site, purification, and characterization. *J Biol Chem.* 258:7155–7160.
- Bauer AL. 2007. A cell-based model exhibiting branching and anastomosis during tumor-induced angiogenesis. *Biophys J BioFAST.* 92:3105–3121.
- Bottenstein JE, Sato GH. 1979. Growth of a rat neuroblastoma cell line in serum-free supplemented medium. *Proc Natl Acad Sci USA.* 76:514–517.
- Capasso V, Micheletti A, Morale D. 2008. Stochastic geometric models, and related statistical issues in tumour-induced angiogenesis. *Math Biosci.* 214:20–31.
- Carosi JA, Eskin SG, McIntire LV. 1992. Cyclical strain effects on production of vasoactive materials in cultured endothelial cells. *J Cell Physiol.* 151:29–36.
- Chaplain MA. 2000. Mathematical modelling of angiogenesis. *J Neurooncol.* 50:37–51.
- Chien S, Li S, Shyy YJ. 1998. Effects of mechanical forces on signal transduction and gene expression in endothelial cells. *Hypertension.* 31:162–169.
- Deroanne CF, Lapiere CM, Nussgens BV. 2001. *In vitro* tubulogenesis of endothelial cells by relaxation of the coupling extracellular matrix-cytoskeleton. *Cardiovasc Res.* 49:647–658.
- Guilkey JE, Hoying JB, Weiss JA. 2005. Large-scale modeling of the mechanical behavior of multicellular constructs. *Proceedings of the ASME Summer Bioengineering Conference*, Vail, CO, June 22–26.
- Guilkey JE, Hoying JB, Weiss JA. 2006. Computational modeling of multicellular constructs with the material point method. *J Biomech.* 39:2074–2086.
- Hoying J, Boswell C, Williams S. 1996. Angiogenic potential of microvessel fragments established in three-dimensional collagen gels. *In Vitro Cell Dev Biol Anim.* 32:409–419.
- Ingber DE. 2002. Mechanical signaling and the cellular response to extracellular matrix in angiogenesis and cardiovascular physiology. *Circ Res.* 91:877–887.
- Ives CL, Eskin SG, McIntire LV. 1986. Mechanical effects on endothelial cell morphology: *in vitro* assessment. *In Vitro Cell Dev Biol.* 22:500–507.
- Jalali S, del Pozo MA, Chen K, Miao H, Li Y, Schwartz MA, Shyy JY, Chien S. 2001. Integrin-mediated mechanotransduction requires its dynamic interaction with specific extracellular matrix (ECM) ligands. *Proc Natl Acad Sci USA.* 98:1042–1046.
- Joung IS, Iwamoto MN, Shiu YT, Quam CT. 2006. Cyclic strain modulates tubulogenesis of endothelial cells in a 3D tissue culture model. *Microvasc Res.* 71:1–11.
- Krishnan L, Hoying JB, Das R, Weiss JA. 2003. Alterations in the material properties of collagen by angiogenesis. *Proc 49th Annu Orthop Res Soc Meet.* 28:278.
- Krishnan L, Ngyuen H, Song H, Hoying JB, Weiss JA. 2005. Gene expression in a three-dimensional model of angiogenesis: relation to matrix mechanical properties. *Proceedings of the ASME Summer Bioengineering Conference abstract b0290109*, Vail, CO, June 22–26.
- Krishnan L, Hoying JB, Nguyen H, Song H, Weiss JA. 2007. Interaction of angiogenic microvessels with the extracellular matrix. *Am J Physiol Heart Circ Physiol.* 293:H3650–H3658.
- Krishnan L, Underwood CJ, Maas S, Ellis BJ, Kode TC, Hoying JB, Weiss JA. 2008. Effect of mechanical boundary conditions on orientation of angiogenic microvessels. *Cardiovasc Res.* 78:324–332.
- Krishnan L, Utzinger U, Maas SA, Reese SP, Weiss JA, Williams SK, Hoying JB. 2009. Extracellular matrix stiffness modulates microvascular morphology during early sprouting angiogenesis *in vitro*. *Proceedings of the ASME Summer Bioengineering Conference SBC2009:206782.*
- Liu Y, Griffith M, Watsky MA, Forrester JV, Kuffova L, Grant D, Merrett K, Carlsson DJ. 2006. Properties of porcine and recombinant human collagen matrices for optically clear tissue engineering applications. *Biomacromolecules.* 7:1819–1828.
- Li S, Huang NF, Hsu S. 2005. Mechanotransduction in endothelial cell migration. *J Cell Biochem.* 96:1110–1126.
- Manoussaki D, Lubkin SR, Vernon RB, Murray JD. 1996. A mechanical model for the formation of vascular networks *in vitro*. *Acta Biotheor.* 44:271–282.
- Mantzaris NV, Webb S, Othmer HG. 2004. Mathematical modeling of tumor-induced angiogenesis. *J Math Biol.* 49: 111–187.
- McCormick SM, Frye SR, Eskin SG, Teng CL, Lu CM, Russell CG, Chittur KK, McIntire LV. 2003. Microarray analysis of shear stressed endothelial cells. *Biorheology.* 40: 5–11.

- Namy P, Ohayon J, Tracqui P. 2004. Critical conditions for pattern formation and *in vitro* tubulogenesis driven by cellular traction fields. *J Theor Biol.* 227:103–120.
- Patrick CW, Jr, McIntire LV. 1995. Shear stress and cyclic strain modulation of gene expression in vascular endothelial cells. *Blood Purif.* 13:112–124.
- Pourdeyhimi B, Dent R, Davis H. 1997. Measuring fiber orientation in nonwovens Part III: Fourier transform. *Textile Res J.* 67:143–151.
- Qutub AA, Popel AS. 2009. Elongation, proliferation & migration differentiate endothelial cell phenotypes and determine capillary sprouting. *BMC Syst Biol.* 3:13.
- Roberts AB, Sporn MB, Assoian RK, Smith JM, Roche NS, Wakefield LM, Heine UI, Liotta LA, Falanga V, Kehrl JH et al., 1986. Transforming growth factor type beta: rapid induction of fibrosis and angiogenesis *in vivo* and stimulation of collagen formation *in vitro*. *Proc Natl Acad Sci USA.* 83:4167–4171.
- Sander EA, Barocas VH. 2009. Comparison of 2D fiber network orientation measurement methods. *J Biomed Mater Res A.* 88:322–331.
- Shepherd B, Chen H, Smith C, Gruionu G, Williams S, Hoying J. 2004. Rapid perfusion and network remodeling in microvascular construct after implantation. *Arterioscler Throm Vasc Biol.* 24:898–904.
- Shiu YT, Weiss JA, Hoying JB, Iwamoto MN, Joung IS, Quam CT. 2005. The role of mechanical stresses in angiogenesis. *Crit Rev Biomed Eng.* 33:431–510.
- Stamatas GN, McIntire LV. 2001. Rapid flow-induced responses in endothelial cells. *Biotechnol Prog.* 17:383–402.
- Sulsky D, Chen Z, Schreyer HL. 1994. A particle method for history dependent materials. *Comput Methods Appl Mech Eng.* 118:179–196.
- Sulsky D, Zhou S, Schreyer HL. 1995. Application of a particle-in-cell method to solid mechanics. *Comput Phys Commun.* 87:236–252.
- Vernon RB, Sage EH. 1999. A novel, quantitative model for study of endothelial cell migration and sprout formation within three-dimensional collagen matrices. *Microvasc Res.* 57:118–133.
- WinFiber3D., available at <http://mrl.sci.utah.edu/>.